6-11-2010

Van Der Waals-London Dispersion Interaction Framework for Experimentally Realistic Carbon Nanotube Systems

Roger H. French
Case Western Reserve University, roger.french@case.edu

Author(s) ORCID Identifier:

iD Roger H. French

Rick Rajter[a], Roger H. French[b]

[a] Massachusetts Institute of Technology, Cambridge, Massachusetts
[b] DuPont Co. Central Research, Wilmington, Delaware

Van der Waals–London dispersion interaction framework for experimentally realistic carbon nanotube systems

A system's van der Waals–London dispersion interactions are often ignored, poorly understood, or crudely approximated, despite their importance in determining the intrinsic properties and intermolecular forces present in a given system. There are several key barriers that contribute to this issue: 1) lack of the required full spectral optical properties, 2) lack of the proper geometrical formulation to give meaningful results, and 3) a perception that a full van der Waals–London dispersion calculation is somehow unwieldy or difficult to understand conceptually. However, the physical origin of the fundamental interactions for carbon nanotube systems can now be readily understood due to recent developments which have filled in the missing pieces and provided a complete conceptual framework. Specifically, our understanding is enhanced through a combination of a robust, ab-initio method to obtain optically anisotropic properties out to 30 electron Volts, proper extensions to the Lifshitz's formulations to include optical anisotropy with increasingly complex geometries, and a proper methodology for employing optical mixing rules to address multibody and multi-component structures. Here we review this new framework to help end-users understand these interactions, with the goal of better system design and experimental prediction. Numerous examples are provided to show the impact of a material's intrinsic geometry, including optical anisotropy as a function of that geometry, and the effect of the size of the nanotube core and surfactant material present on its surface. We'll also introduce some new examples of how known trends in optical properties as a function of [n, m] can result in van der Waals interactions as a function of nanotube classification, radius, and other parameters. The concepts and framework presented are not limited to the nanotube community, and can be equally applied to other nanoscale or even biological systems.

Keywords: Carbon nanotubes; van der Waals

1. Introduction

Van der Waals–London dispersion (vdW–Ld) interactions arising from quantum electrodynamics (QED) are of considerable importance to scientists and engineers across many disciplines. First, they are influential in behaviors ranging from colloidal interactions in solution to the fracture behavior of bulk materials [1]. Second, the vdW–Ld interactions are even influential when so-called "stronger" forces, such as electrostatic or polar interactions, are present [2]. And finally, they are universally long range interactions that can only be nullified by carefully designing the system to balance the attractive and repulsive components of the overall interaction [3]. Thus the study of van der Waals–London dispersion spectra (vdW–LDS) and forces can enrich our understanding of particular phenomena, which is important for scientists and engineers interested in using self-assembly processes to create nanoscale structures and devices.

But despite being important and of interdisciplinary interest, vdW–Ld interactions calculated from a first principles, QED approach (i. e., the Lifshitz formulation [4]) have a reputation for being intractable or difficult to use and understand. Thus it is very common to use outdated pairwise models with Lennard–Jones potentials, ignoring the fundamental electrodynamics and the important many-body effects. Admittedly, there are two barriers that can still prevent people from getting started:

1. the lack of the full spectral optical properties of all the components within the system, and
2. the lack of an analytically tractable solution for the system geometry of interest. While both of these are still issues today, much progress has been made on both fronts in the past 20 years [1 – 3, 5].

First, the formulations have been extended to include everything from an infinite number of layers (stacked in the semi-infinite half-space formulation), to optically anisotropic solid cylinders interacting with each other in salt solutions [6]. Recently the formulations for solid cylinders were extended even further in order to incorporate optical anisotropy into the solid cylinder–cylinder and cylinder–substrate formulations at the near and far-limits. The ability to combine all these new features is essential for metallic single-wall carbon nanotubes (SWCNTs) due to the large degree of optical anisotropy coupled with their large morphological aspect ratios [7]. And we are by no means limited to just rods and flat planes. A recent book published by Parsegian also contains a large array of vdW–Ld formulations for different geometries [3].

Second, the advent of robust, fast, and reliable ab-initio codes has allowed for the calculation of full spectral optical properties for materials which are either very difficult or impossible to quantitatively measure experimentally. Experimental methods like vacuum ultraviolet (VUV) reflec-

tivity for bulk optical properties [8], transmission valence electron energy loss spectroscopy (VEELS) for interfacial optical properties [8], or reflection VEELS for surfaces [9] are still useful for the characterization of many materials. But for nanoscale materials like SWCNTs, techniques like EELS result in many inherent inaccuracies in the anisotropic spectral optical properties because of the difficulty in isolating, aligning, measuring and then analyzing the measured signals off a single SWCNT. Thus ab-initio computations of full spectral optical properties eliminate this barrier by offering a way to obtain this data for nanoscale materials with results that are directly comparable.

With the introduction of ab-initio optical properties and Lifshitz formulations designed for SWCNTs, it is now possible to begin calculating vdW–Ld interactions for a limited number of systems (i. e., systems containing SWCNTs only with no surfactant). However, a crucial piece is still needed to address all potential system variations relevant for experimentalists (e. g., surfactant coated SWCNTs, multi-wall CNTs, and SWCNTs having a very large core volume [17]). For planar systems, this issue was alleviated by the introduction of the "add-a-layer" approach [1] in which the 3-component solution was expanded to include an infinite number of parallel layers of arbitrary ordering and thickness. The boundary conditions of parallel planes made this a straightforward process after the initial expansion was generated [3]. Unfortunately, the cylindrical geometries have no equivalent analytical form to include such layer stacking as a function of cylinder radius. And without the ability to address this radial spatial variation, the effects of

ssDNA (single-stranded DNA), SDS (sodium dodecyl sulfate), and other well known surfactants would have to be ignored.

Fortunately there is a viable alternative to an add-a-layer formulation. Spectral mixing to produce effective medium spectra [10] for use at the appropriate surface-to-surface separation limits can be used to create effective vdW–LDS that results in an exact total vdW–Ld energy. In principle, this is no different than if we took a highly spatially resolved optical spectra of water (clearly oxygen and hydrogen locations have different quantities of electrons and wave functions) and averaged it back to the isotropic value that has been thoroughly studied and used for decades [3, 11–14].

With the ab-initio optical properties [15], optically anisotropic cylinder formulations [7, 16], and mixing formulations for SWCNT systems now in place [17], a full framework for calculation of the vdW–Ld interactions for SWCNTs is now available. This is summarized in the flow chart found in Fig. 1. To see the actual optical spectra and vdW–Ld properties as they relate to SWCNTs through the steps in the flow chart, see Figs. 2 and 3, which track these properties from the chirality indices [n, m] to the angular dependent Hamaker coefficients (the material component of the total vdW–Ld energy) for the [6,5,s] semiconducting and [9,3,m] metal SWCNTs. The vdW–Ld framework presented here is being implemented in Gecko Hamaker, a free and open source software package which contains optical properties and various geometrical formulations appropriate to vdW–Ld interaction science [19].
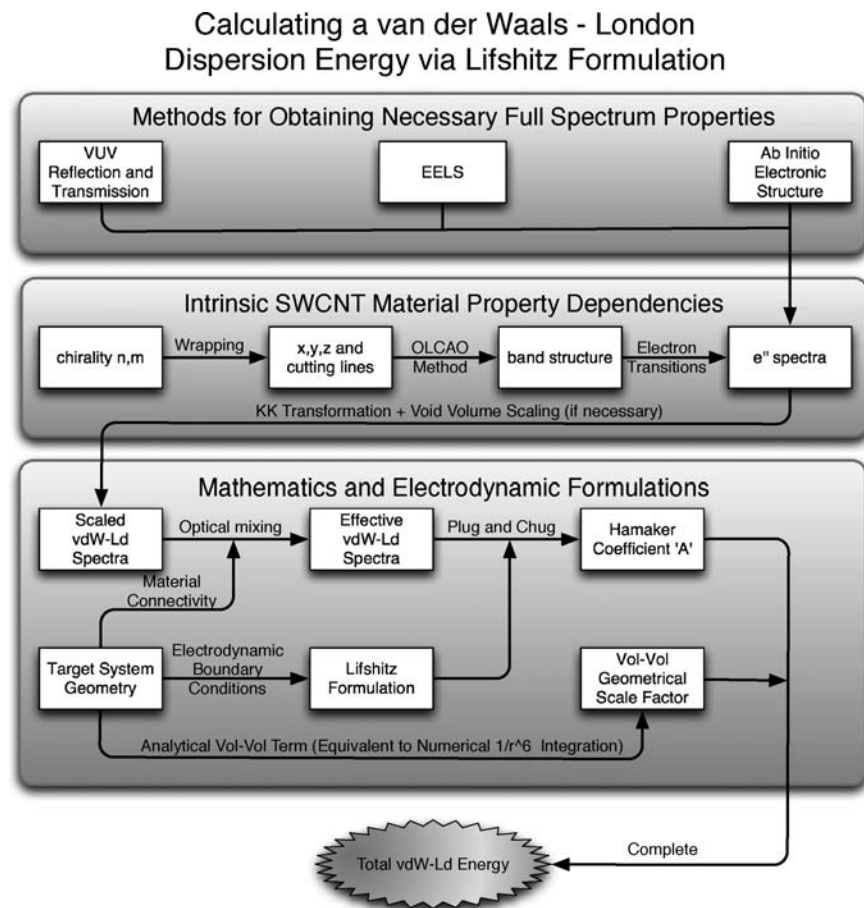

Fig. 1. The complete flow chart of the Lifshitz formulation/framework that is necessary for calculating and understanding the physical origin of the chirality-dependent Hamaker coefficients and vdW–Ld total energies of SWCNT systems.
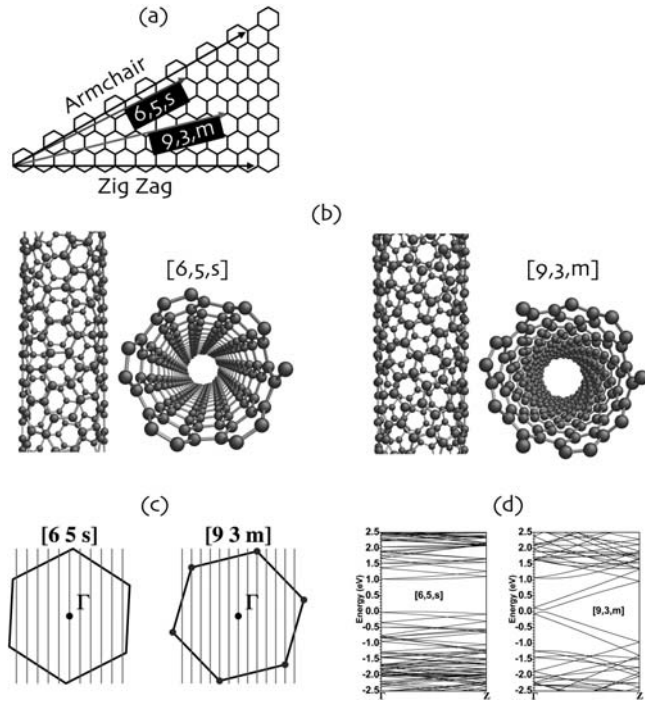
Fig. 2. Part 1 of the chirality-dependent vdW–Ld interaction analysis for the [6,5,s] and [9,3,m]. (a) The [n, m] vector placed upon the graphene sheet denotes the circumference of the SWCNT. (b) The SWCNTs x, y, z positions in space. Note the structural difference in the twisting. (c) The cutting lines within the Brillouin zone, varying in quantity and angle based on the specific [n, m] magnitudes and magnitude ratio between them. (d) The band diagrams determined by the allowable states along the cutting lines. Stages E through G are continued in Fig. 3.
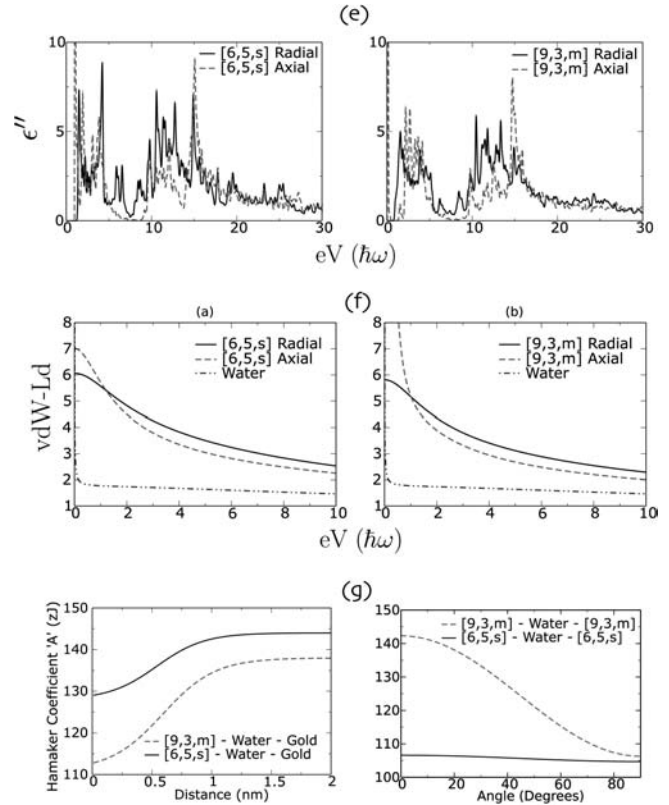

Fig. 3. Part 2 of the chirality-dependent vdW–Ld interaction analysis for the [6,5,s] and [9,3,m]. (e) The allowable single electron transitions determine the optical absorption part of the dielectric spectrum, $\varepsilon''(\omega)$, over all real frequencies. (f) The vdW–LDS obtained via the KK transform upon $\varepsilon''(\omega)$. Note the differences between a SWCNTs radial and axial directions as well as the differences between the tubes. (g) Hamaker coefficients in a solid cylinder SWCNT–water–gold substrate system as a function of ℓ. Additional and/or later stages include an analysis of DOS/JDOS as well as total vdW–Ld energies.

What follows is an end-user tutorial highlighting key features within Fig. 1 as they relate to Figs. 2 and 3. Although determining vdW–Ld interactions for SWCNT systems tends to be more complicated than isotropic plane–plane systems, the overall form of the Lifshitz calculation remains common across many types of geometries of increasing complexity. Numerous examples are included to demonstrate the major effects of varying optical properties, Lifshitz geometry, and mixing rules in order to guide the reader. Finally, we include some emerging results from our upcoming data-mining analysis across 63 SWCNTs. The optical properties as a function of radius and metallic/semiconducting classification trend in both obvious and surprising ways when carried through to the final Hamaker coefficients and total energies.

2. Background

2.1. vdW–Ld Theory

A brief overview of the link from optical properties [20] to Hamaker coefficients is useful before comparing and contrasting the different vdW–Ld formulations [3]. The key source of all vdW–Ld interactions is optical contrast between each system interface. The index of refraction (an optical property) serves as a useful proxy for the dispersion or polarizability in this discussion, while the vdW–Ld interaction is based more accurately on another optical property, the London dispersion spectra, across a wider range of frequencies. If there were no optical contrast in the universe,

then all materials would be equally polarizable and all electromagnetic radiation would move from phase to phase, passing through a variety of interfaces or boundaries the same way. Without optical contrast, there would be no preferential placement of particular objects and hence no vdW–Ld interaction to lower the system's free energy. But optical contrast does exist among different materials and over a wide range of optical frequencies. It is this contrast that opens the door for attractive and repulsive vdW–Ld interactions depending upon the many possible components in a system.

2.1.1. Buoyancy illustration

A buoyancy illustration can be quite helpful in understanding the many-body vdW–Ld interaction at its most primitive level. In Fig. 4, we note that the two different blocks of materials rest on the ground in air. If we were to try and separate these blocks along the vertical axis, gravity would pull the blocks back down towards one another. This is similar to any two materials in vacuum. They are each more polarizable in air than when compared to the vacuum, and thus "fall" towards each other in order to minimize the system's energy.

The many-body nature of the interaction becomes apparent when we add water (the medium) to a system with one block of a higher density and one of a lower density than
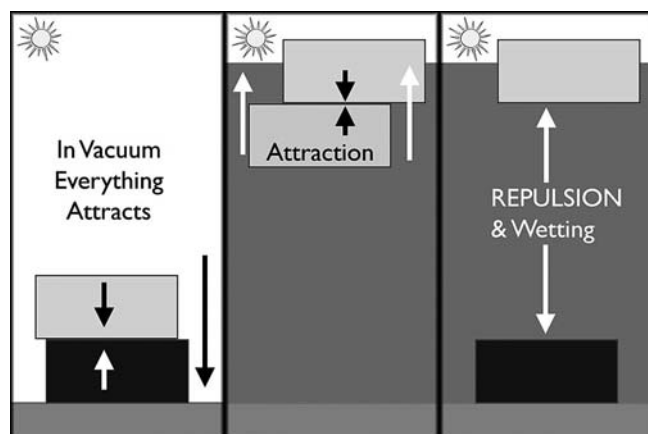
Fig. 4. An illustration relating the similar effects of optical contrast in a far-limit vdW–Ld interaction with that of density contrast (i.e. relative buoyancy). It is the relative contrast between all components that determines whether there is a net attraction or repulsion between any 2 given components in the overall system. Material density is indicated by color with white being vacuum and black or very dark colors being the most dense.

the water (Fig. 4 part C). In this situation, there is a "repulsive" force between the two blocks as a result of one sinking and one floating in the liquid medium. Other blocks added would rise or sink depending on their own respective buoyancies. A similar effect occurs with the vdW–Ld interactions. If the medium's optical properties (e.g., index of refraction) is intermediate to that of the two objects, the system will minimize its overall energy by moving those two objects far apart. But if both materials either have lower or higher indices of refraction than the water medium, they will attract towards each other again. This is equivalent to the interacting blocks both being more or less dense than the water and driving towards one another. In either case, attraction between A and B only occurs if the medium is either more or less dense than each object present.

We could extend the buoyancy analogy further to describe more complicated phenomena. For instance, we could change the medium's density by adding an additional component or changing the temperature. An example of this is a Galileo thermometer [21], where changes in temperature create a change in the ambient liquid density. The temperature indicators (of a relatively fixed density versus temperature) then begin to rise/fall as this change occurs. Another extension of the buoyancy analogy is that of a multi-component system, such as a boat. While the outer shell of an oil tanker is far more dense than the water, the total density over the entire ship is such that the boat floats. The effect is similar for vdW–Ld forces, where the magnitude and percent volume of the components present dictate the overall attraction to planes of higher and lower optical density.

There are, however, a few areas where the buoyancy illustration and a vdW–Ld interaction are not truly analogous. The first is that vdW–Ld interactions arise from optical contrast across ALL optical frequencies as opposed to buoyancy's reliance on a single term (weight density). What this means is that a vdW–Ld interaction between objects in a system can have both attractive and repulsive parts for a given medium and materials A and B. Yet the interaction at a given frequency is still identical to a snapshot of relative buoyancy. It is therefore essential to consider all

the frequencies in the electrodynamic interaction, not to oversimplify to one or a few interaction frequencies. This is due to the fact that the entire frequency range contributes to the overall Lifshitz summation, with a bulk of this contribution coming from frequencies of higher energy than visible light.

The analogy is also not consistent when considering the behavior of the system as the medium's thickness or the separation distance changes. Buoyancy does not show manybody effects which vary as a function of separation distances. But the vdW–Ld interaction has a fundamental scaling of the separation distance and the optical penetration depth (sampling depth), or the interaction volume of the two bodies which determines what parts of the two bodies are dominating the interaction at a given separation. For example in the near limit, where the separation of the two bodies is much smaller than their size, then the surface of the two bodies is controlling, while at long separation distances the average properties of the whole bodies is important. This is mainly a result of the inverse power-law scaling of the total vdW–Ld interaction energy. Understanding how the different components of each body contribute as a function of the surface-to-surface separation is an important departure from the buoyancy analogy, which is equivalent to the far-limit.

Despite its shortcomings, the buoyancy illustration is a conceptually easy to understand model that can be useful in understanding the quantitative and qualitative impact of each component within the full Lifshitz framework (Fig. 1). Upon a closer analysis of these interdependencies, one can have a better understanding of the fundamental workings of the interactions and thereby make smarter decisions on experimental design.

3. The fundamental framework

3.1. Ab-initio optical properties

If the source of a van der Waals interaction is optical contrast at all system interfaces, then it is imperative to obtain the optical spectra for all the components present in the system to the highest accuracy possible. This typically requires having the imaginary part of the dielectric function (ε'' spectra) for each material over an interval from $0 - 30$ electron volts (eV) to ensure complete convergence. The way that the particular optical properties are obtained is only relevant if there are particular caveats to consider, such as a particular frequency/energy range where the data tend to not be certain. Beyond that, the various experimental or ab-initio optical properties are interchangeable. For example: some choose to view the results in $J_{cv}(eV)$ form (interband transition strength) while others prefer dielectric function over real frequencies ($\varepsilon''(\omega)$). The choice really depends upon the optical property features that are under investigation because $J_{cv}(eV)$ and $\varepsilon''(\omega)$ weight the peaks differently. One can convert between the two via the following:

$$J_{cv}(eV) = \frac{m_o^2}{e^2\hbar^2}\frac{eV^2}{8\pi^2}(\varepsilon''(eV) + \imath\varepsilon'(eV)) \tag{1}$$

Where $J_{cv}(eV)$ is proportional to the interband transition probability and has units of $g \cdot cm^{-3}$. For computational

convenience, we take the prefactor $m_o^2 e^{-2} \hbar^{-2}$ in Eq. (1), whose value in cgs units is $8.29 \cdot 10^{-6} \text{ g} \cdot \text{cm}^{-3} \cdot \text{eV}^{-2}$, as unity [1]. For vdW–Ld calculations, the optical data needs to be converted into vdW–LDS. Assuming ε'' is properly scaled to the correct magnitude, this is done using the following form of the Kramers–Kronig (KK) transformation: [3, 15, 20].

$$\varepsilon(\imath\xi) = 1 + \frac{2}{\pi} \int_0^\infty \frac{\varepsilon''(\omega) * \omega}{\omega^2 + \xi^2} \, d\omega \qquad (2)$$

We refer to $\varepsilon(\imath\xi)$, a real function over the imaginary frequency domain, as the vdW–Ld spectrum (or vdW–LDS) in order to differentiate it from the dielectric function over real frequencies ($\varepsilon''(\omega)$). Although the $\varepsilon(\imath\xi)$ form of the optical spectra appear to be simple damped oscillators, they contain the complete electronic structure and interatomic bonding of the materials, i.e., the interband transitions that determine the optical properties. Additionally, small differences in both the magnitude and stacking order of the vdW–LDS in a geometrical configuration can influence both the magnitude and the sign of the total vdW–Ld interaction energy. For our SWCNT calculations, we use the ε'' properties, obtained from ab-initio orthogonal linear combination of atomic orbital (OLCAO) computations [22–27], that have been scaled to the solid and hollow cylinder geometries [17].

One final issue should be addressed before moving on. Some researchers may have concerns over the usage of ab-initio optical properties for fear that they may be inaccurate or unrealistic in comparison to experimental data. A typically cited concern is the discrepancy that exists between experiment and theory in band gap calculations, particularly for models that employ simplifications like the tight binding approximation. However, vdW–Ld interactions are dependent upon all the electronic transitions, with significant transitions occurring in the deep UV ranges up to 30 eV and higher. The full OLCAO calculation captures this correctly because it contains complete orbital information up to the 4p and 3d shells. The results have compared very well to experimental ε'' data and Hamaker coefficient calculations for systems like graphite, ZrO_2, AlN, LiB_2O_3 and including organic materials with hydrogen such as polysilane [23–27]. This gives us confidence in using this data for systems like SWCNTs, which we believe to be very difficult to accurately obtain experimentally because of the small size and cylindrical shape of these materials. By using an ab-initio method, we can easily and systematically calculate the optical properties for all possible SWCNT types.

As for the actual method, the primary equation for obtaining $\varepsilon''(\omega)$ from the band structure is as follows [22–26]:

$$\varepsilon_{ij}''(\omega) = \frac{4\pi^2 e^2}{\Omega m^2 \omega^2} \sum_{knn'\sigma} \langle kn\sigma|p_i|kn'\sigma\rangle \langle kn'\sigma|p_j|kn\sigma\rangle f_{kn}(1 - f_{kn'})$$
$$\delta(e_{kn'} - e_{kn} - \hbar\omega) \qquad (3)$$

Here again $\varepsilon''(\omega)$ is the imaginary part of the dielectric spectrum at a given frequency ω, with mass m, and Brillouin zone volume Ω. The momentum operators, p_i and p_j, operate on both the valence and conduction band wave functions, where the i and j subscripts represent the directions of the tensor in three dimensional space. The Fermi function (f_{kn}) terms ensure that only transitions between an occupied valence to an unoccupied conduction band transition are allowed, and the delta function ensures that only transitions corresponding to the particular energy $\hbar\omega$ are considered.

This is simply the ab-initio way of obtaining the data. There are also various experimental results which provide excellent corroboration. As an example, Stephan et al. have done impressive work obtaining experimental ε'' data for SWCNTs along the axial direction by applying a grazing angle EELS measurement [28]. Despite some noise in the data and the lack of chirality/direction identification, the ε'' results corroborate many of the key features (most notably the large ε'' peaks around 15 eV) of the present authors' ab-initio data. New results published just last year add support for these peak positions and magnitudes [29]. The energy loss function determined from EELS data, though useful for qualitative corroboration, cannot itself be used for the calculation of certain properties (e.g., a vdW–Ld interaction) because it is arbitrarily scaled along its y-axis and thus lacks the necessary quantification. But having both the experimental and ab-initio properties gives us quantitative data that we can confidently use because of their agreement. These fundamental optical properties can then be used for predictive experimental design schemes for systems using dielectrophoresis (DEP) or having sensitive vdW–Ld interactions.

Figure 5 shows the ab-initio dielectric function ε'' using Eq. (3) for both the [6,5,s] and [9,3,m] SWCNTs in their axial and radial directions obtained previously [7]. We then used Eq. (2) to obtain the vdW–Ld spectra as shown in Fig. 6. The metallic [9,3,m] SWCNT has a considerable amount of anisotropy, particularly at energies near 0 eV when the axial direction shoots up to a value of 333.

The most notable features in Figs. 5 and 6 are the variations that exist as a function of direction and chirality. Since
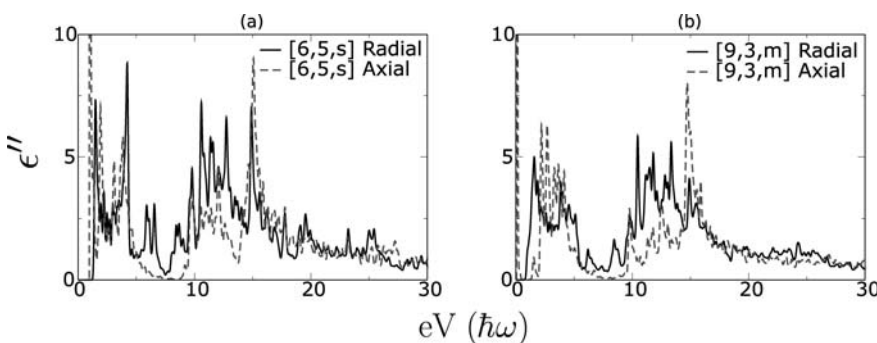

Fig. 5. The ε'' spectra of the (a) [6,5,s] and (b) [9,3,m] SWCNTs scaled to a solid cylinder geometry. The metallic [9,3,m] SWCNT axial direction spikes to a value of 930 at 0.04 eV.
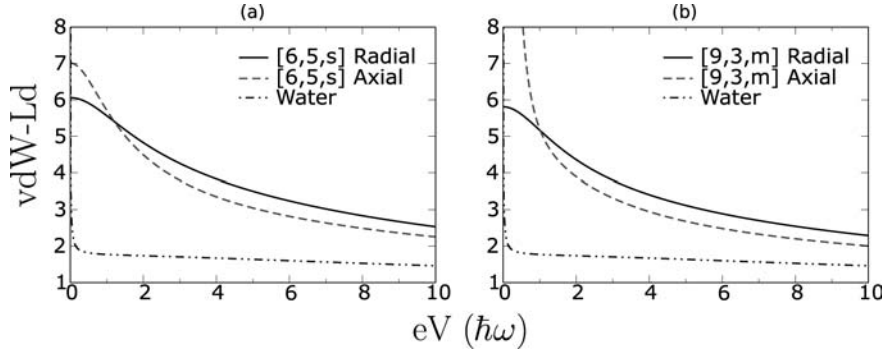
Fig. 6. The vdW–Ld spectra of the (a) [6,5,s] and (b) [9,3,m] SWCNTs scaled to a solid cylinder geometry and compared to the index matching water spectra. The [9,3,m] axial direction spikes up to a value of 333 at 0 eV.

the vdW–LDS are the very inputs to the full Lifshitz formulation, one can observe a clear possibility for a chirality-dependent vdW–Ld interaction. Of course, the magnitude of such an interaction needs to be determined.

3.2. Lifshitz formulations

Once we have the vdW–Ld spectra for the materials within a given system, the Lifshitz formulation weights their optical contrast contributions at the required Matsubara frequencies and determines the vdW–Ld interaction strength by a single Hamaker coefficient $\mathcal{A}$. The Hamaker coefficient (which is approximately the volume–volume vdW–Ld interaction density or strength between two components of a system) is then multiplied by the proper geometrical scale factor to determine the vdW–Ld interaction energy or force. Thus the general form of the vdW–Ld energy is [3, 15]:

$$\mathcal{G} = -\mathcal{A} \cdot \frac{g}{\ell^n} \tag{4}$$

where $\mathcal{G}$ is the thermodynamic free energy, g is a collection of geometry factors (e.g. $g = \pi a^2/6$ per unit of cylinder length for the far-limit, cylinder–substrate geometry where a is the nanotube radius), and ℓ^n is the scaling law behavior at a surface-to-surface separation distance ℓ for a given geometry. Essentially $\mathcal{A}$ is the interaction strength as a function of the material properties of two objects within the given geometry, whereas g and n depend solely by the system geometry itself. Geometry affects the magnitude of the Hamaker coefficient because the optical contrast functions change as a function of geometry in the Lifshitz summation, and cannot be decoupled into a strictly material-dependent explanation. To demonstrate this coupling further, we shall observe the change of the optical contrast functions as a function of increasing geometrical complexity, ranging from the simple isotropic plane–plane geometry to the cylinder–cylinder interactions relevant for SWCNT systems.

The calculation of $\mathcal{A}$ for the non-retarded case[1] over all three levels of complexity has a consistent general form:

$$\mathcal{A}^{NR} = \frac{3k_b T}{2} * \frac{1}{2\pi} \sum_{n=0}^{\infty} {}' \int_0^{2\pi} \Delta_{\mathcal{L}m} \Delta_{\mathcal{R}m} \mathrm{d}\varphi \tag{5}$$

where n denotes the discrete Matsubara frequencies ($\xi_n = \frac{2\pi k_b T}{\hbar} n$) ranging from 0 to ∞, the values $\Delta_{\mathcal{L}m}$ and

---

[1] In the non-retardedc case, we neglect the finite speed of light traveling back and forth between the interacting sides.
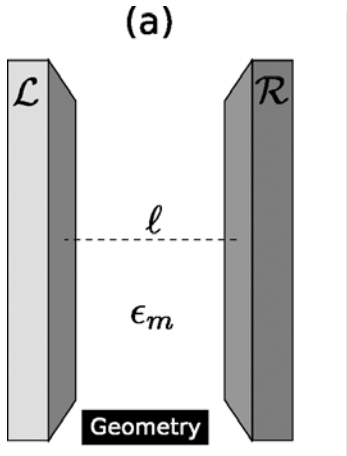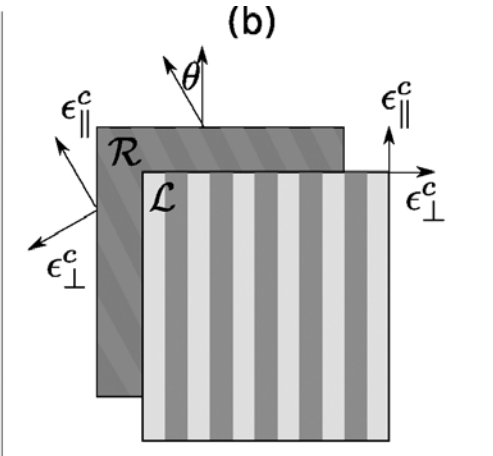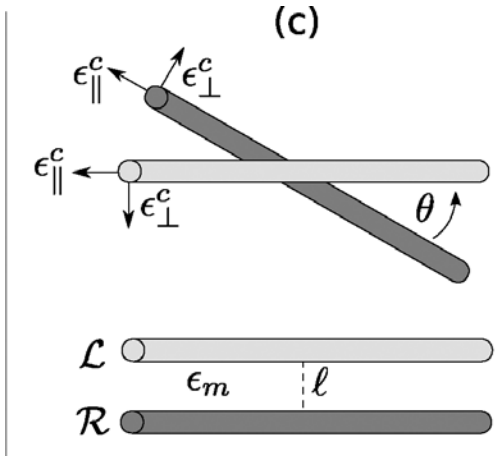
$\Delta_{\mathcal{R}m}$ are the spectra mismatch functions comparing the vdW–Ld spectra properties of the particular material $\mathcal{L}$ or $\mathcal{R}$ with the neighboring medium m. The prime on the summation denotes that the first frequency $n = 0$ is multiplied by 0.5.

It is with this general form that we can compare all three systems (Fig. 7). When looking at this figure, pay special attention to how the components of spectral mismatch functions (i.e. $\Delta_{\mathcal{L}m}$ and $\Delta_{\mathcal{R}m}$) vary as a function of the geometry. Changes in the forms of these weighting functions can have a substantial impact in changing the sign and magnitude of the overall interaction.

3.2.1. Optically isotropic planar system

The isotropic plane–plane system (see Fig. 7a) is the most commonly used of all the Lifshitz formulations because it is by far the easiest to calculate and it is the most relevant for the interactions of large bulk materials. Its energy per unit area is

$$\mathcal{G} = \frac{\mathcal{A}^{NR}}{12\pi\ell^2} \tag{6}$$

Because the left and right half-spaces are both isotropic, there is no angular dependance of the vdW–Ld interaction for rotations about the interface normal of either half space. Therefore the integration around angle $\mathrm{d}\varphi$ leads to constant value of 2π which cancels out the $\frac{1}{2\pi}$ coefficient in the general form to leave us with

$$\mathcal{A} = \frac{3k_b T}{2} \sum_{n=0}^{\infty} {}' \Delta_{\mathcal{L}m} * \Delta_{\mathcal{R}m} \tag{7}$$

The $\Delta_{\mathcal{L}m}$ and $\Delta_{\mathcal{R}m}$ terms are as follows

$$\Delta_{\mathcal{L}m}(\imath\xi_n) = \frac{\varepsilon_{\mathcal{L}}(\imath\xi_n) - \varepsilon_m(\imath\xi_n)}{\varepsilon_{\mathcal{L}}(\imath\xi_n) + \varepsilon_m(\imath\xi_n)}$$

$$\Delta_{\mathcal{R}m}(\imath\xi_n) = \frac{\varepsilon_{\mathcal{R}}(\imath\xi_n) - \varepsilon_m(\imath\xi_n)}{\varepsilon_{\mathcal{R}}(\imath\xi_n) + \varepsilon_m(\imath\xi_n)} \tag{8}$$

We normally drop the explicit $(\imath\xi_n)$ notation for clarity as it is assumed that all vdW–Ld spectra are frequency dependent and only calculated at each Matsubara frequency (ξ_n) (where each n represents a change of 0.16 eV for the case of 300 K). These mismatch terms all have an $\frac{a-b}{a+b}$ form, which can never exceed a value of 1 because the

Fig. 7. The 3 different systems of comparison. (a) Isotropic semi-infinite half spaces (b) Anisotropic semi-infinite half spaces (c) Anisotropic solid cylinders. The energy $\mathcal{G}$ is in units of per nm^2 of substrate area in a) and b) versus per nm of cylinder in c).

vdW–LDS cannot have values below unity. Thus there is a maximum possible contribution at any given frequency in the summation over all frequencies.

3.2.2. Optically anisotropic planar system

As we move to the next level of complexity we eliminate the assumption of isotropic spectral optical properties and allow the substrates to have optically uniaxial properties, with vdW–Ld spectra for the parallel $\varepsilon_\parallel$ and perpendicular directions to the optical axis. In our particular derivation, we confine the formulation to only allow rotations of the optical axis within the plane of the interface (see Fig. 7b). This restriction leads to the appropriate geometrical formulation for a SWCNT interacting with a packed array of aligned SWCNTs [7]. In principle, one can arrange the two substrates so $\varepsilon_\parallel$ has an arbitrary relationship to the interface and leads to a component normal to the planar interface.

Because of the angular dependance that arises, the overall vdW–Ld energy now has two components $\mathcal{A}^{(0)}$ and $\mathcal{A}^{(2)}$.

$$\mathcal{G} = -\frac{\mathcal{A}^{(0)} + \mathcal{A}^{(2)} \cos^2 \theta}{12\pi\ell^2} \quad (9)$$

Here $\mathcal{A}^{(0)}$ represents the Hamaker coefficient when the left and right half-space have their optical axes ($\varepsilon_\parallel$) 90 degrees out of phase with respect to one another. As θ, the angle between the optical axes of the left and right half spaces, goes

to 0, we get an additional energy contribution from $\mathcal{A}^{(2)}$. $\mathcal{A}^{(0)}$ can be calculated by itself, but the angular contribution is calculated by taking the aligned case ($\mathcal{A}^{(0)} + \mathcal{A}^{(2)}$) and subtracting off $\mathcal{A}^{(0)}$. The form for both endpoints is created by adding the angular dependance to the generalized form to get:

$$\mathcal{A}^{(0)} = 3k_bT2 * 12\pi \sum_{n=0}^{\infty}{}' \int_0^{2\pi} \Delta_{\mathcal{L}m}(\varphi)\, \Delta_{\mathcal{R}m}(\varphi - \pi/2)\, \mathrm{d}\varphi \quad (10)$$

$$\mathcal{A}^{(0)} + \mathcal{A}^{(2)} = 3k_bT2 * 12\pi \sum_{n=0}^{\infty}{}' \int_0^{2\pi} \Delta_{\mathcal{L}m}(\varphi)\, \Delta_{\mathcal{R}m}(\varphi)\, \mathrm{d}\varphi \quad (11)$$

Now we need to consider the detailed forms of $\Delta_{\mathcal{L}m}$ and $\Delta_{\mathcal{R}m}$ and how these are calculated for this scenario. They are as follows:

$$\Delta_{\mathcal{L}m}(\varphi) = \left(\frac{\varepsilon_\perp(\mathcal{L})\sqrt{1 + \gamma(\mathcal{L})\cos^2\varphi} - \varepsilon_m}{\varepsilon_\perp(\mathcal{L})\sqrt{1 + \gamma(\mathcal{L})\cos^2\varphi} + \varepsilon_m} \right) \quad (12)$$

$$\Delta_{\mathcal{R}m}(\varphi) = \left(\frac{\varepsilon_\perp(\mathcal{R})\sqrt{1 + \gamma(\mathcal{R})\cos^2\varphi} - \varepsilon_m}{\varepsilon_\perp(\mathcal{R})\sqrt{1 + \gamma(\mathcal{R})\cos^2\varphi} + \varepsilon_m} \right) \quad (13)$$

$$\Delta_{\mathcal{R}m}(\varphi - \pi/2) = \left(\frac{\varepsilon_\perp(\mathcal{R})\sqrt{1 + \gamma(\mathcal{R})\sin^2\varphi} - \varepsilon_m}{\varepsilon_\perp(\mathcal{R})\sqrt{1 + \gamma(\mathcal{R})\sin^2\varphi} + \varepsilon_m} \right) \quad (14)$$

where γ, a measure of the optical anisotropy for the left or right half-spaces in the near limit, is of the form

$$\gamma = \frac{\varepsilon_\parallel - \varepsilon_\perp}{\varepsilon_\perp} \tag{15}$$

If the parallel and perpendicular epsilons are equivalent, then $\gamma = 0$ and the above Δ terms reduce to Eq. (8).

3.2.3. Optically anisotropic solid cylinders

Things get more interesting and complex when we change the geometry of the system from two interacting planar substrates to interacting cylinder substrates. The energy is now on a per unit length basis for two parallel aligned SWCNTs of diameter a_1 and a_2

$$G(\ell, \theta = 0) = -\frac{3(\pi a_1^2)(\pi a_2^2)(\mathcal{A}^{(0)} + \mathcal{A}^{(2)})}{8\pi\ell^5} \tag{16}$$

or as total energy when the two SWCNTs are misaligned

$$G(\ell, \theta) = -\frac{(\pi a_1^2)(\pi a_2^2)(\mathcal{A}^{(0)} + \mathcal{A}^{(2)}\cos^2\theta)}{2\pi\ell^4 \sin\theta} \tag{17}$$

Next we need a determination of $\mathcal{A}$. If we move towards solid cylinders far away from a substrate, we can use the *Pitaevskii* method [3] for dilute rods in solution and deduce the relevant $\Delta_{\mathcal{R}m}$ and $\Delta_{\mathcal{L}m}$ terms. The derivation is tedious, but straightforward [6, 7, 44]. The result is

$$\Delta_{\mathcal{L}m}(\varphi) = -\left(\Delta_\perp(\mathcal{L}) + \tfrac{1}{4}(\Delta_\parallel(\mathcal{L}) - 2\Delta_\perp(\mathcal{L}))\cos^2\varphi\right) \tag{18}$$

$$\Delta_{\mathcal{R}m}(\varphi) = -\left(\Delta_\perp(\mathcal{R}) + \tfrac{1}{4}(\Delta_\parallel(\mathcal{R}) - 2\Delta_\perp(\mathcal{R}))\cos^2\varphi\right) \tag{19}$$

$$\Delta_{\mathcal{R}m}(\varphi - \pi/2) = -\left(\Delta_\perp(\mathcal{R}) + \tfrac{1}{4}(\Delta_\parallel(\mathcal{R}) - 2\Delta_\perp(\mathcal{R}))\sin^2\varphi\right) \tag{20}$$

where

$$\Delta_\parallel = \frac{\varepsilon_\parallel - \varepsilon_m}{\varepsilon_m} \qquad \Delta_\perp = \frac{\varepsilon_\perp - \varepsilon_m}{\varepsilon_\perp + \varepsilon_m} \tag{21}$$

Although these Δ terms are different in appearance from the previous two formulations, the calculations are just as straightforward from a computational standpoint. However, it is within these newly introduced anisotropic terms $\Delta_\parallel$, $\Delta_\perp$, and γ that new and interesting phenomena arise, which we will discuss in more detail later. A quick numerical comparison of these different parts elucidates the impact of these mismatch functions, particularly for highly optically anisotropic tubes like the [9,3,m]. Table 1 shows how they impact the $n = 1$ (0.16 eV at room temperature) Matsubara frequency for the [6,5,s] and [9,3,m] in water.

A few things to note. The only spectral mismatch terms that exceed unity are γ, $\Delta_\parallel$, and the far-limit $\Delta_{\mathcal{L}m}$. All other spectra mismatch functions typically do not come close to this limit except those with a very large optical contrast (i.e., a difference of 1+ orders of magnitude in relative optical strength). Although γ itself can be large and contribute to both the total and orientation-dependent energies, its location under the square root signs in Eqs. (12–14) dampens its effect. Thus even for the highly anisotropic [9,3,m], the contribution of $\mathcal{A}^{(2)}$ at the near limit is 1.11 zJ (typical near-limit Hamaker coefficients of SWCNTS in water are

Table 1. A comparison of how the various spectral mismatch components contribute to the overall Hamaker coefficient for the [6,5,s] and [9,3,m] SWCNTs at the first Matsubara frequency ($n = 1$ or approximately 0.16 eV at room temperature).

	[6,5,s]	[9,3,m]
ε_m	2.02	2.02
$\varepsilon_\parallel$	6.96	18.27
$\varepsilon_\perp$	6.05	5.77
γ	0.15	2.17
$\Delta_\perp$	0.50	0.48
$\Delta_\parallel$	2.45	8.05
$\Delta_{\mathcal{L}m}$ Near	0.53, 0.50	0.67, 0.48
$\Delta_{\mathcal{L}m}$ Far	0.86, 0.50	2.25, 0.48
$\mathcal{A}^{(0)}, \mathcal{A}^{(2)}$ Near (zJ)	1.08, 0.82	1.47, 1.11
$\mathcal{A}^{(0)}, \mathcal{A}^{(2)}$ Far (zJ)	1.83, 1.52	6.05, 7.80

above 60 zJ). The $\Delta_\parallel$ term, in comparison, results in a contribution of 7.8 zJ for $\mathcal{A}^{(2)}$ (see Table 1).

3.3. Spectral mixing for realism

As noted earlier, an add-a-layer solution for the cylindrical geometries does not, at this time, appear to be analytically tractable. Despite this limitation, experimentalists and theoreticians need some way to quantitatively address the effects of cylindrical multi-layered systems. To resolve this tension, approximations need to be carefully applied in order to balance the needs of the end-users without introducing unrealistic artifacts into the formulations.

Figure 8 shows several systems of interest for experimentalists, ranging from a single solid cylinder to coated SWCNTs and multi-wall carbon nanotubes (MWCNTs). The systems can be made even more complex by using non-uniform surfactant coverage or non-concentric MWCNTs, but we shall stick to the simpler cases in order to cleanly illustrate a proper strategy. The major difference between these systems from a vdW–Ld standpoint is that the optical properties vary spatially as a function of radius. Understanding the radial dependence of the optical properties in the far-limit (surface-to-surface separation greater than two cylinder diameters) is necessary to calculate the total energy and the Hamaker coefficients, which respectively depend on the interacting volume size and optical properties contained within that volume. Ideally one would do this via an add-a-layer approach like the one used in plane–plane geometries, including an arbitrary quantity of layers of materials of arbitrary thickness [1, 3, 19, 30, 31].
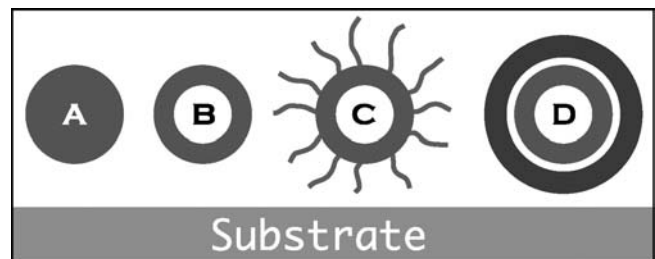

Fig. 8. The many levels of interactions with a substrate. (a) A solid cylinder (b) a hollow cylinder (c) a hollow cylinder coated with a surfactant and (d) a hollow cylinder within a cylinder.

But, at present, no such formula appears to exist or is readily obtainable.

Fortunately, we can use effective spectra in each limiting case (near/far-limits) such that the solid-cylinder formulations can be used without loss of realism; the chief concern when using this or any approximation. To use the solid-cylinder formulations and not sacrifice accuracy, one needs two primary inputs: 1) The optical properties of all the constituent materials (medium + SWCNT + outer surfactant + core material). 2) A sensible spectral mixing formulation that gives effective averaged optical spectra for the entire object. The only remaining issue is whether such a mixing rule is equally valid across all separation distances. It turns out that the two limiting separation distances (what we refer to as the near and far limits) require different treatments, which we'll detail next.

3.3.1. Spectral mixing considerations at the near-limit

For all geometrical arrangements at the near-limit (i.e., less than 0.5 nm surface-to-surface separation), the vdW–Ld properties of the surfaces on each material tend to dominate the interaction because of the divergent behavior of the total energy scaling, thus no mixing is required. This is well known for plane–plane geometries [3] (see Appendix Figs. 14 and 15 for qualitative and quantitative examples). However, it is worth illustrating this point further because it is critical to our assertion that while spectral mixing is not acceptable practice at the near limit, it is viable and necessary at the far limit if no analytical formulations exist. This demonstration is included as Appendix B.

3.3.2. Spectral mixing considerations at the far-limit

The study of vdW–Ld interactions for SWCNTs at the far limit is particularly exciting from an optical anisotropy standpoint because the $\Delta_\parallel = \dfrac{\varepsilon_\parallel - \varepsilon_m}{\varepsilon_m}$ term within the Hamaker coefficient summation can go over unity when $\varepsilon_\parallel \gg \varepsilon_m$. Without this restriction, each Matsubara frequency in the Lifshitz summation is no longer capped at maximum contribution value and can result in Hamaker coefficient variation as a function of chirality and orientation [3, 7]. In terms of spectral mixing considerations, we are no longer dealing with distances approaching contact and therefore must average the optical properties to get an effective solid cylinder. Typically the spectral mixing of optical properties is done via an effective medium approximation (EMA), such as Bruggeman EMA [32]. The basic form is as follows:

$$\sum_i \varphi_i \frac{\varepsilon_i - \varepsilon}{\varepsilon_i + 2\varepsilon} = 0 \tag{22}$$

Where φ_i is the volume fraction of each component. From a physical standpoint, the unmodified Bruggeman EMA lacks any predominant geometrical arrangement of material connectivity in a particular direction. One can make a case that the radial direction of a SWCNT also lacks a predominant geometrical arrangement. If we slice a cross-section and discretize it into small units, some parts would behave like a series capacitor and others (e.g., the circumferential

portions within the cylindrical shell) would behave more like capacitors in parallel. Therefore, using either of the endpoints (e.g., series or parallel capacitor mixing) would not be a valid approach and the Bruggeman EMA appears to be the best balance (see Fig. 9).

In the axial direction, the polarization can easily be split into well defined regions of continuous connectivity. Therefore a cross sectional area weighting (i.e., a parallel capacitor averaging) is valid. This is particularly important for the metallic SWCNTs, which tend to have a very large (100+) vdW–Ld spectra peak at 0 eV. If we used the EMA mixing rule, the axial direction spectra at 0 eV would be artificially lowered and the $\Delta_\parallel$ terms would not contribute as strongly to the overall total energy.

Figure 10 compares the effects of the parallel capacitor, Bruggeman EMA, and series capacitor mixing formulations for two materials with varying volume fractions. When the optical properties of two materials at a given frequency are very close in magnitude, the variation among the three models is quite small. However, in the situations where there is a large optical contrast, the parallel capacitor model evenly weights the two spectra by volume fraction while the Bruggeman EMA is considerably damped by the weakest of the two or more spectra magnitudes. The series and parallel capacitor methods represent the limiting cases of connectivity while the Bruggeman and other EMAs can be thought of as intermediate arrangements of the material connectivity in 3D space.

It should be noted that there are many other mixing formulations available, such as Lorentz–Lorenz, Maxwell–Garnett, and Rayleigh. However, Lorentz–Lorenz assumes a vacuum host instead of any arbitrary medium or addi-
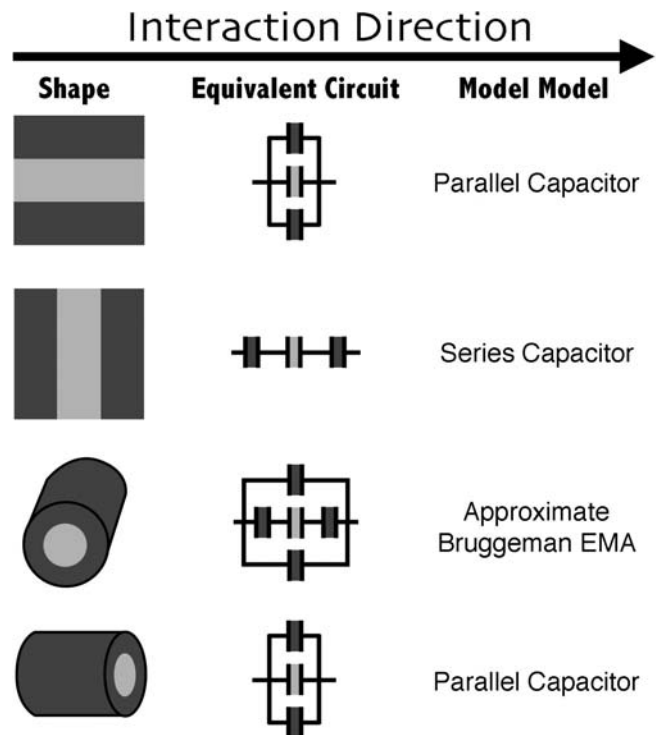

Fig. 9. A comparison of various material configurations with the equivalent capacitor circuits and mixing model equivalents. The radial direction for the SWCNT system is the only arrangement that does not have an "exact" equivalent, with the Bruggeman EMA being the best known fit.

R. Rajter, R. H. French: Van der Waals–London dispersion interaction framework
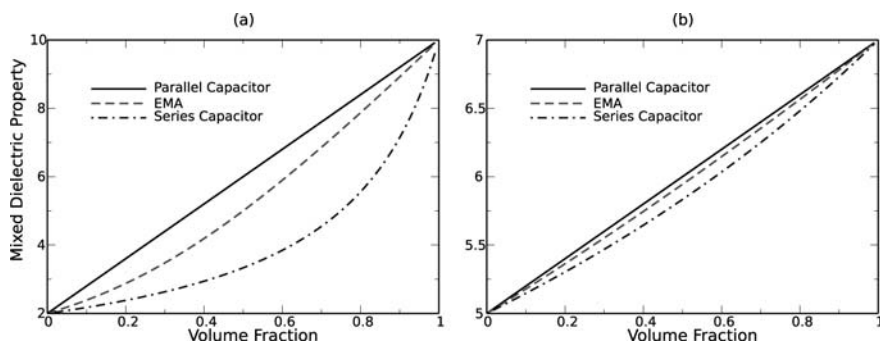

Fig. 10. Comparison of the parallel capacitor, Bruggeman EMA, and series capacitor spectral mixing approximations. (a) When the magnitude of one spectrum is many times larger than the other (which is typical in the DC or 0 eV limit of metallic SWCNTs), the different models exhibit more variation as the connectivity becomes important. (b) When the optical spectra are similar in magnitude, all three models converge to similar values for any volume fraction, and therefore the choice of which particular mixing formulation to use is less of an issue.

tional materials. This would be insufficient to create a MWCNT out of two or more SWCNT components. Maxwell–Garnett assumes a dilute volume fraction within the host material. While the SWCNTs can certainly be dilute in the water medium, the mixing formulation itself is done within the confines of the other shell layer of the SWCNT, therefore not really dilute from that perspective. Rayleigh mixing tends to give far too much weight to the weaker of the two spectra, closely representing the effects of the series capacitor, which is also not ideal for SWCNTs.

The Bruggeman EMA mixing formulation tends to be the most appropriate for our SWCNT systems because it doesn't assume which material is the host (i.e. dominant or majority material) or assume a predominant connectivity. If such a situation did arise where one needed additional connectivity in the radial direction, but not quite reaching the parallel limit, straightforward interpolations are available to achieve every gradation in between [32]. In short, the Bruggeman EMA can be interpolated to all of the other models with a simple q factor varying from 0 (zero screening parallel capacitor) to 1 (series capacitor). We use the traditional Bruggeman EMA for the purposes of this paper, but leave the door open for further refinements on this q factor if it is needed in certain situations.

To quantify the impact of the mixing formulations, Table 2 compares the effects of 6 different mixing rules on a 50–50 mixture of the [25,0,s] radial direction with vacuum. This particular SWCNT was chosen because it does not have a metallic 0 eV behavior and its core void space is almost exactly 50 % of the total volume of the entire SWCNT + core. Therefore, this tube will maximize the relative magnitude variation between the mixing rules (by being an even 50–50 ratio) and not introduce any changes as a result of a divergent low energy wing in the vdW–LDS. The parallel and series capacitor methods are still

the endpoints, resulting in the largest and smallest possible magnitudes respectively. The Maxwell–Garnett model resides between the EMA and parallel capacitor and the Lorentz–Lorenz and Raleigh models are much closer to the series capacitor model. The variation between these different models is quite large. Both the Hamaker coefficients and the effective vdW–Ld spectra can vary by a factor of 3. Therefore, it is important to choose the model carefully for a given geometrical system, particularly for complex and multi-component systems.

Figure 11 shows the [9,3,m] and [29,0,s] SWCNT hollow-cylinder spectra and the resulting mixed with H_2O spectra in the axial direction using isotropic water uniformly distributed and filling 100 % of each SWCNTs respective core. Of course the core can be filled with any percentage of water from 0 to 100 %. In this study, we assume a 100 % of filling of isotropic order to have a standard benchmark across all tubes. If we were using the smallest of constructible nanotubes (e.g. the [5,0,s]), any water filling would not be possible as there is not enough void space to fit the water molecules. A slightly larger diameter would allow for some water molecules, but they would not have all rotational degrees of freedom and the assumption of the isotropic spectra would not hold. The tubes presented in this study are large enough that these issues should not arise. But if they did and one could determine the proper degree of water filling and optical anisotropy, the same analysis would be straightforward and easily achievable.

Table 2. A comparison of the effects of the different mixing formulations on a 50–50 mixture of the [25,0,s] radial direction and vacuum.

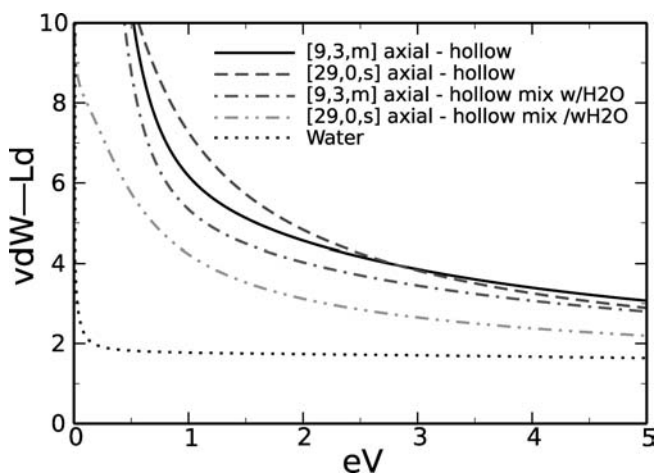| Mixing Formulation	vdW–Ld (0 eV)	vdW–Ld (1 eV)	$\mathcal{A}_{121}$
Parallel Capacitor	5.87	3.84	82.10
Perpendicular Capacitor	1.83	1.74	29.84
Bruggeman EMA	4.21	3.02	63.90
Maxwell Garnett	5.00	3.37	53.28
Lorentz–Lorenz	2.86	2.46	70.23
Rayleigh	2.42	2.17	44.92

Fig. 11. Here we see the hollow-cylinder and the hollow-cylinder spectra mixed w/H_2O for the [9,3,m] and [29,0,s] SWCNTs in the axial direction. Note that the [9,3,m] spectra only shift a little while the effect upon the [29,0,s] is much more dramatic because of its substantially larger core volume.

Although there are many alternative water spectra from which to choose [11–14], we use the index of refraction oscillator model by Parsegian because it accurately captures the zero frequency, matches index of refraction along the visible frequencies [3], and is easily recreated using simple damped oscillators. The other available models do make certain improvements (such as fulfilling the requirements of the *f*-sum rule [14], etc) and are equally valid for use. In general, the water spectrum is smaller in magnitude than the all-SWCNT spectra for all frequencies. This has the effect of decreasing the overall magnitude of the effective, mixed w/H_2O spectra in comparison to the hollow-cylinder spectra. The effect is clearly strong for the [29,0,s], which is 55 % hollow and therefore experiences a considerable shifting. (The [9,3,m], by comparison, is only 18 % hollow). The implications of this dampening show up clearly in the Hamaker coefficient calculations between the various chiralities (Table 3). However, effects such as alignment and torque forces may increase or decrease depending on the relative positioning on the initial and final vdW–Ld spectra. In the particular examples found in this paper, they all diminish.

Although not specifically included in this paper, there is no additional conceptual, computational difficulty to include surfactants in this analysis. For example: a MWCNT with a water core and a uniform layer of sodium dodecyl sulfate (SDS, a typical SWCNT surfactant [33]) would simply behave as a cross-sectional area weighted by mixing of the constituent spectra in the far-limit and of pure SDS at the near-limit. One could then use the interpolation style suggested previously to obtain a vdW–Ld energy at all distances [7].

The biggest limitation for including surfactant effects is, as described earlier, the lack of optical spectra for all potential surfactant candidates over an energy range sufficient for the Lifshitz formulations. There is work being done in parallel to this thesis to fill up the spectra database, but more time and resources are needed. Until robust spectral data are available, it is difficult to take this analysis further, other than to describe qualitative trends that can occur. At the near-limit, the ability to spatially resolve the optical properties of the SDS layer (i.e. the surfactant) from the SWCNT interior is just as important as being able to resolve the SWCNT constituents contained within a MWCNT (as opposed to the bulk averaged MWCNT optical properties).

Experimental methods that determine bulk spectral properties of ssDNA/SWCNT hybrids and similar nano-structures would be pertinent for the far-limit only. The near-limit requires a spatial resolution and possibly directionally

dependent properties, both of which are either impossible or extremely difficult to obtain experimentally for these types of systems. Specific examples are the situations in which the structure in water is different from the dry material structure (e.g. DNA). If one measured a dry structure, but later calculated an energy for a wet system, there might be some significant shifts or alterations based on the different electronic structure. This further underscores the utility of ab-initio methods as a viable and powerful alternative to obtain this information. Additionally, it underscores the need to catalogue even the most basic of materials. Currently the only organic materials we have publicly available (outside of the carbon based SWCNTs) are polystyrene, polysilane, tetradecane, ethanol, and possibly a few others [34–36]. With a larger data base of SWCNTs and surfactant spectra, one can start data mining to find combinations favorable for one type of interaction over another [18].

4. Discussion (systematic trends for SWCNTs)

There are several great overview articles to describe the intricate relationships between [n, m], cutting lines, band structure, and total density of states (DOS). (See [37–43].) Fortunately, the ε'' trends occur as a function of chirality, potentially leading to trends in the overall Hamaker coeficients and total vdW–Ld as a function of SWNCT classification and radius. Although a complete analysis is beyond the scope of this paper, a few key examples will be introduced to prove the point.

The armchair SWCNTs (where the [n, m] indices are identical) are the easiest and best class on which to do this analysis: 1) There is no change in the cutting line angle among them. Therefore, it isolates the resulting vdW–LDS effects to the known ε'' vHS (van Hove singularity) shifts in the 0–5 eV range. The 10–30 eV range (largely cutting angle dependent) remains fixed and unchanged down to the smallest diameter SWCNTs. 2) They are all metals from a band structure standpoint and thus all the vHS will be large and have systematic shifts relative to one another. 3) Pragmatically it is easy to calculate/obtain a very large number of this class of SWCNTs because of their relatively small lattice repeat length along the axial direction in the OLCAO supercell calculation. Of the 63 SWCNT ε'' spectra that we presently have, 22 are armchair tubes ranging form the [3,3,m] to the [24,24,m]. Chiral SWCNTs, by comparison, can require 1–3 orders of magnitude more atoms and thereby become computationally prohibitive with what is readily obtainable on a reasonable budget.

Table 3. Calculated cylinder–cylinder Hamaker coefficients ($\mathcal{A}^{(0)}$, $\mathcal{A}^{(2)}$) for the [6,5,s] and [9,3,m] SWCNTs using the raw optical properties scaled to a solid cylinder, scaled to a hollow cylinder, and a hollow cylinder mixed with a water core. The solid and mixed w/H_2O spectra are equally valid at the far-limit depending on whether the core is filled with vacuum or water.

		Near-limit $\mathcal{A}^{(0)}$, $\mathcal{A}^{(2)}$ (zJ)			Far-limit $\mathcal{A}^{(0)}$, $\mathcal{A}^{(2)}$ (zJ)		
n	m	Solid	Hollow	Mixed w/H_2O	Solid	Hollow	Mixed w/H_2O
9	3	62.3, 0.5	91.7, 0.6	66.7, 0.5	107.0, 36.2	163.3, 56.6	113.3, 36.8
6	5	85.0, 0.1	111.8, 0.1	88.0, 0.1	105.6, 1.9	144.2, 3.3	110.5, 2.2
9	1	72.3, 0.4	95.6, 0.4	75.3, 0.3	92.8, 3.0	126.9, 4.9	97.4, 3.3
29	0	14.3, 0.0	71.8, 0.1	20.1, 0.1	18.5, 0.8	108.6, 8.6	26.2, 1.3
Validity at this limit		No	Yes	No	Yes	No	Yes

There are essentially three ways that manipulations in ε'' effects vdW–LDS: shape, position, and area. The two components that have the most impact are area (pulls the entire vdW–LDS spectra up or down linearly as a function of ε'' scaling) and position (shifts in ε'' change the vdW–LDS slope at the high and low energy wings). With the ε'' trending and peak behavior now identified, we can analyze and understand the fundamental reasons as to why vdW–LDS trend and behave as they do and ultimately link from [n, m] to vdW–Ld interactions.

Note the distinct ε'' trending regimes in Fig. 12. The peaks above the invariant 4.19 eV peak are all locked in position, shape, and magnitude. The peaks from $0-4$ eV depend on the cutting line density in the Brillouin zone and systematically shift lower with increasing radius while slightly increasing the total area under the curve. This slight increase in area makes sense in terms of balancing the fsum rule's effective electron density [20], which scales as $\omega * (\varepsilon'')^2$. So to maintain the same total of electrons, any total shift of a ε'' peak to a lower energy should raise its ε'' value in order to maintain a fixed quantity of valence electrons. It is yet another great confirmation between optical property theory, SWCNT trending, and the OLCAO calculations.

If we simply had the ε'' spectra in Fig. 12, the following effects would be expected: 1) The vdW–LDS for the largest tubes would have the sharpest slope near the low energy limit and remain lower and flatter in the higher energy limit as the vHS shift to a lower energy. 2) The slight increase in ε'' area for the larger tubes in the $0-4$ eV regime would slightly increase the overall magnitude of the vdW–LDS across some of the energy interval. 3) These first two effects would be additive in the low energy regime and would combat each other in the high energy interval. A close inspection of Fig. 12 reveals that all of these effects are occurring just as expected from Eq. (2). These trends in vdW–LDS would therefore carry over as trends in the Lifshitz summation and lead to the chirality-dependent Hamaker coefficients and vdW–Ld interactions.

Before continuing, it is useful to develop a naming system in order to identify the main peaks and describe the ε'' peaks, trends, and features in a sensible way. Observing graphene's partial DOS (see Fig. 13), it is clear that the 0 to 5 eV transitions can only come out of the $\pi-\pi$ interactions. For transitions of 10 eV or more, a significant portion of the transitions in the TDOS should be coming from the σ bonds (for graphene, all σ bonds are assumed to be sp2 hybridized with no sp3 characteristics). A major drop in available DOS in the π states below -7.5 eV in the conduction band would support this thesis.
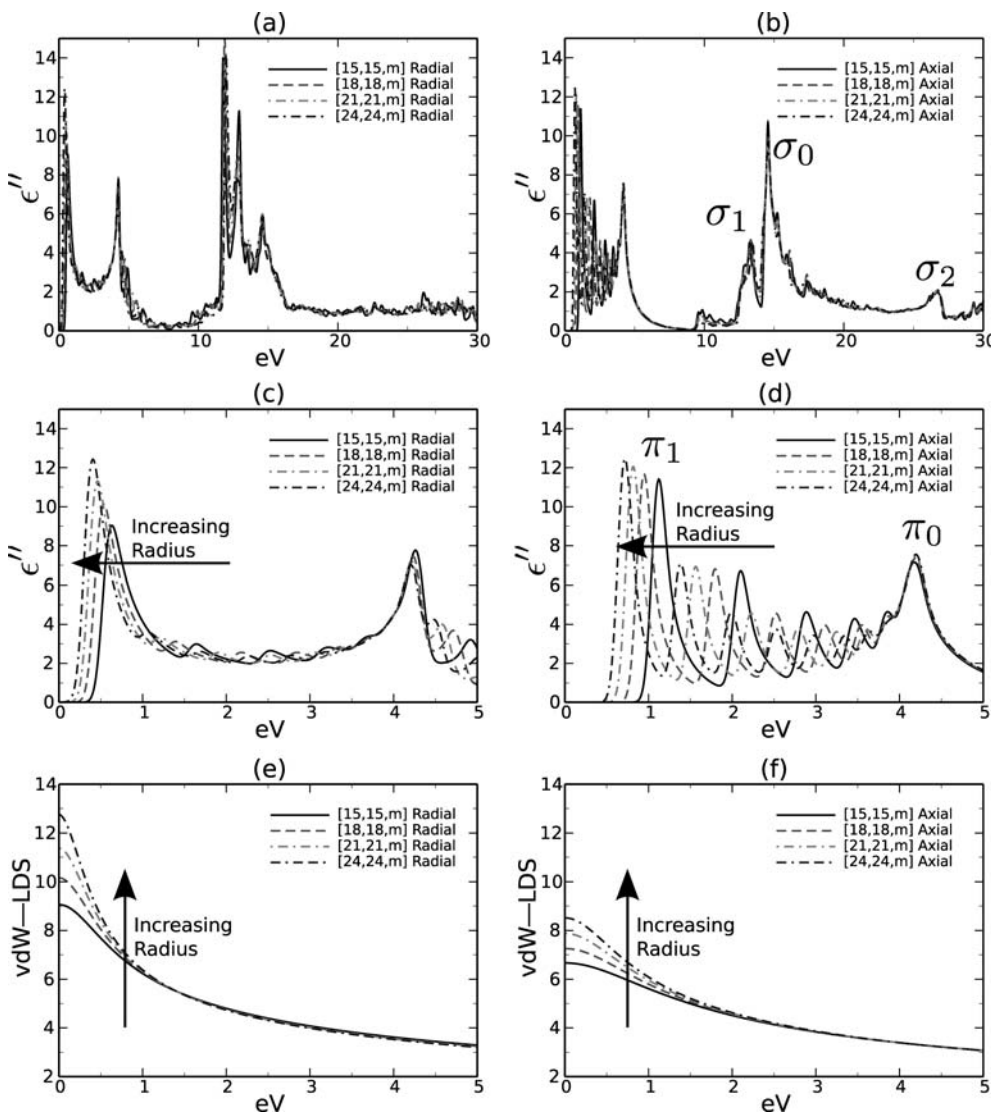

Fig. 12. A comparison of the ε'' and vdW–LDS trends in the radial and axial directions for armchairs SWCNTs ranging from the [15,15,m] to the [24,24,m].
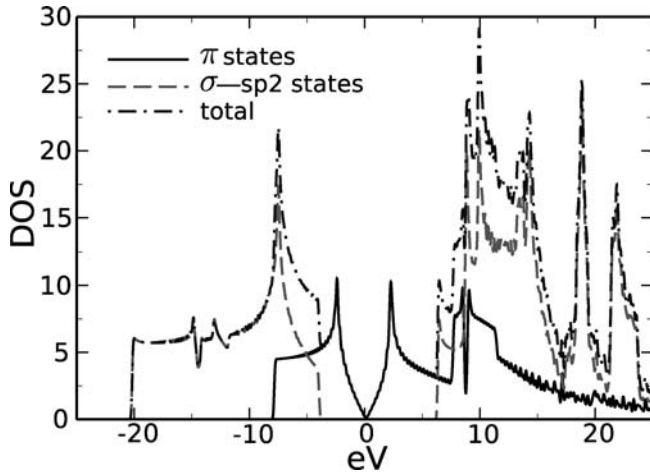
Fig. 13. The total DOS of graphene compared to the partial DOS components within the plane (sp$_2$ hybridized bonding) and out of the plane (π bonds).

Combining the graphene partial DOS study with the ε'' peak analysis in Fig. 12, we can make the following claims: the 0–5 eV peaks are described entirely by the π–π bonds while the 5–30 peaks are dominated by a combination of π–$\sigma*$, σ–$\pi*$, and σ–$\sigma*$ bonds. Of course, larger diameter tubes have little to no curvature in the circumferential direction and thus little to no σ–π overlap. Therefore it is likely that the transitions will arise more from σ–σ transitions until the diameters are below a critical transition radius where the curvature becomes much stronger.

There is another piece that has been missing, and that is the possibility for a Drude metal peak in the optical properties at 0 eV. The word "possibility" is key because simply having a continuos DOS in a band structure does not imply ε'' activity in that same energy interval (as can be seen in Fig. 13, which compares graphene's partial DOS and ε'' spectra). Such ε'' transitions can be prohibited due to symmetry effects. Simply put, there is a possibility that some "metal" SWCNTs can behave optically like a semi-conductor. However, metals that do have near 0.00 eV ε'' transitions can exhibit some dramatic effects because of this large, low energy wing (e.g. vdW–Ld torques that have a preferred alignment direction along the axial direction [7]).

In short, there are three major peak regimes: Drude, σ, and π. But more granularity is needed to describe the peaks within these domains. We use "peak" to describe any location in ε'' that exhibits a rise and fall of 1 unit within a +/− 0.5 eV range of position. Although shoulders (i.e. locations in the spectra that abruptly rise or fall to a new plateau) are equally important features in optical property analysis, we will confine ourselves to peaks for the time being because of the ease with which we can automate identification.

There are many different ways we could label the peaks within each regime. We could correlate to the known CNT vHS, order them from lowest to highest, or order them by strength, etc. Ultimately we found this scheme to be the most beneficial: Drude, π, and σ labels to represent transitions in the energy ranges of 0.0–0.1, 0.1–10, and 10+ eV respectively.

For the Drude metal range, there are three major types observed. There is either no low energy ε'' peak present (i.e. it is optically a 1+ eV semiconductor), or a metallic ε'' wing sharply rising all the way to 0.00 eV, or a nearly metallic ε'' wing sharply rising to almost 0.00 eV before termi-

nating back to zero at energies around 0.02 to 0.05 eV. To differentiate these three cases, there will be one of three descriptors: null, D0 (true Drude metal down to 0.00 eV), or D1 (spike terminates just short of 0.00 eV).

The next peaks to identify are the π bonds. Both the axial and radial directions have special peaks that are somewhat invariant among the largest diameter SWCNTs. They occur at 4.21 and 4.19 eV, respectively, and are essentially pinned. The remaining peaks vary systematically with the cutting lines. The peak at 4.2 eV is a special peak and is called π_0 to denote its fixed nature. The next significant peak is the optical band gap. We label the next peaks π_1 through π_5. Again the criterion for a peak is a 1 unit increase in ε'' within a range of 0.5 eV on each side.

In the axial direction, we get π_1–π_5 and they systematically shift as a function of $1/r$. The radial direction only has two significant peaks, π_0 and π_1. In both the radial and axial direction, the position of the π_0 peak among the all chiralities remains stable for tubes above a critical radius of approximately 0.8 nm. Below this limit, the magnitude of π_0 is no longer stable and varies considerably among the smaller diameter tubes.

It should be noted that these π_1–π_5 peaks are not necessarily in full agreement with the vHS band-to-band transitions found in the DOS for SWCNTs. In the vHS convention, E_{11} would denote the DOS and ε'' peaks arising from the closest non-Drude metal cutting line to the K-point. E_{22} would denote the second, and so forth. The results are very clean and symmetric, but not directly interpretable; some of these peaks would not transition to the ε'' properties. Therefore, the labeling of the π peaks should not be construed as transitions coming from a particular cutting line or band.

The last set of peaks left is the σ peaks. Much like the π_0 peaks, the σ peaks tend to be invariant until the diameter is very small, introducing geometrical and electronic structure distortions. In general, three major σ peaks are seen. Here we don't use ascending order, but overall ε'' area. The σ_0 peak tends to be around 14.5 (changes slightly based on geometry) with a sister σ_1 peak around 13 eV. Some SWCNT geometries (e.g. armchair) have another more rounded peak around 27 eV. Others (zigzag) do not.

Therefore, the first three σ peaks represent the largest peak in these vicinities (with σ_2 potentially absent). The remaining peaks that arise for very small diameters are not easy to systematically name because they can be sharp and disappear by the next chirality. If we introduced a larger resolution step size in the ε'' calculation (e.g. 0.05 eV instead of 0.01 eV), many of these peaks would simply disappear. Therefore, we feel it is better to simply lump those collectively as $\sigma*$ because their significance depends on the context of the question to be answered.

With these new descriptors in place, we can adequately and quantitatively describe the differences in the five vdW–Ld classifications. This will be the source of exploitable differences in upcoming datamining papers. Original input properties, intrinsic trends as a function of [n, m], formulations versus geometry, and mixing will play a role in this more extensive analysis.

5. Conclusions

SWCNTs are a unique classification of materials where [n, m] can have a profound impact on the Hamaker coeffi-

cient and resulting total vdW–Ld energy. Properly extending the Lifshitz formulations makes it possible to explore this rich, diverse set of interactions, which is experimentally exploitable and will assist in system design. Effects like chirality and angular dependance upon the overall vdW–Ld interaction would be missed if one simply used parameterized and pairwise Lennard–Jones potentials to determine the vdW–Ld energies. The formulations and analysis presented should allow any end-user to determine the vdW–Ld for a wide variety of nanotube systems, as well as many other fields of interest (e.g. bio-molecules, pharmaceuticals, etc.)

References

[1] R. French: J. Am. Ceram. 83 (2000) 2117–2146.
[2] R. French, A. Parsegian, R. Podgornik, R. Rajter, A. Jagota, J. Luo, D. Asthagiri, M. Chaudhury, Y. Chiang, S. Granick, S. Kalinin, M. Kardar, R. Kjellander, D. Langreth, J. Lewis, S. Lustig, D. Wesolowski, J. Wettlaufer, W. Ching, M. Finnis, F. Houlihan, O. von Lilienfeld, C. van Oss, T. Zemby: Rev. Mod. Phys, in Press (2009).
[3] A. Parsegian: Van der Waals Forces, Cambridge University Press, Cambridge (2005).
[4] E. Lifshitz: Sov. Phys. JETP 2 (1956) 73–83.
[5] R. French, R. Cannon, L. DeNoyer, Y. Chiang: Solid State Ionics, 75 (1995) 13–33. DOI:10.1016/0167-2738(94)00217-G
[6] R. Podgornik, A. Parsegian: Phys. Rev. Lett. 80 (1998) 1560–1563. DOI:10.1103/PhysRevLett.80.1560
[7] R. Rajter, R. Podgornik, A. Parsegian, R. French, W. Ching: Phys. Rev. B 76 (2007) 045417. DOI:10.1103/PhysRevB.76.045417
[8] G. Tan, M. Lemon, R. French, D. Jones: Phys. Rev. B 72 (2005) 205117. DOI:10.1103/PhysRevB.72.205117
[9] G. Tan, L. DeNoyer, R. French, M. Guittet, M. Gautier-Soyer: J. of Electron Spectroscopy and Related Phenomena 142 (2004) 97–103. DOI:10.1016/j.elspec.2004.09.002
[10] D. Bruggeman: Ann. Phys. 24 (1935) 636. DOI:10.1002/andp.19354160705
[11] H. Ackler, R. French, Y. Chiang: J. Colloid Interface Sci. 179 (1996) 460–469. DOI:10.1006/jcis.1996.0238
[12] C. Roth, A. Lenhoff: J. Colloid Interface Sci. 179 (1996) 637–639. DOI:10.1006/jcis.1996.0261
[13] R. Dagastine, D. Prieve, L. White: J. Colloid Interface Sci. 231 (2000) 351–358. PMid:11049685; DOI:10.1006/jcis.2000.7164
[14] J. Fernandez-Varea, R. Garcia-Molina: J. Colloid Interface Sci. 231 (2000) 394–397. PMid:11049689; DOI:10.1006/jcis.2000.7140
[15] R. Rajter, R. French, W. Ching, W. Carter, Y. Chiang: J. Appl. Phys. 101 (2007) 054303. DOI:10.1063/1.2709576
[16] R. Rajter, R. French: J. of Phys. Conf. Series: 94 (2008) 012001. DOI:10.1088/1742-6596/94/1/012001
[17] R. Rajter, R. French, R. Podgornik, W. Ching, A. Parsegian: J. Appl. Phys. 104 (2008) 053513. PMCid:2685217; DOI:10.1063/1.2975207
[18] R. Rajter, Ph.D. Thesis, MIT (2009).
[19] http://sourceforge.net/projects/geckoproj
[20] F. Wooten: Optical Properties of Solids, Academic Press, New York (1972).
[21] http://en.wikipedia.org/wiki/Galileo_thermometer
[22] W. Ching: J. of Amer. Ceram. Soc. 73 (1990) 3135–3160. DOI:10.1111/j.1151-2916.1990.tb06430.x
[23] R. French, S. Glass, F. Ohuchi, Y. Xu, W. Ching: Phys. Rev. B 49 (1994) 5133–5142. DOI:10.1103/PhysRevB.49.5133
[24] W. Ching, Y. Xu, R. French: Phys. Rev. B 54 (1996) 13546–13550. DOI:10.1103/PhysRevB.54.13546
[25] Y. Xu, W. Ching, R. French: Phys. Rev. B 48 (1993) 17695–17702. DOI:10.1103/PhysRevB.48.17695
[26] Y. Xu, W. Ching: Phys. Rev. B 51 (1995) 17379–17389. DOI:10.1103/PhysRevB.51.17379
[27] S. Loughin, R. French, W. Ching, Y. Xu, G. Slack: Appl. Phys. Lett. 63 (1993) 1182–1184. DOI:10.1063/1.109764
[28] O. Stephan, D. Taverna, M. Kociak, K. Suenaga, L. Henrard, C. Colliex: Phys. Rev. B 66 (2002) 155422. DOI:10.1103/PhysRevB.66.155422
[29] A. Marinopoulos, L. Reining, A. Rubio: Phys. Rev. B 78 (2008) 235428. DOI:10.1103/PhysRevB.78.235428
[30] K. van Benthem, G. Tan, R. French, L. Denoyer, R. Podgornik, A. Parsegian: Phys. Rev. B 74 (2006) 205110. DOI:10.1103/PhysRevB.74.205110
[31] R. Podgornik, R. French, A. Parsegian: J. Chem. Phys. 124 (2006) 044709. PMid:16460202; DOI:10.1063/1.2150825
[32] H. Fujiwara, J. Koh, P. Rovira, R. Collins: Phys. Rev. B 61 (2000) 10832–10844. DOI:10.1103/PhysRevB.61.10832
[33] C. Richard, F. Balavoine, P. Schultz, T. Ebbesen, C. Mioskowski: Science 300 (2003) 775–778. PMid:12730595; DOI:10.1126/science.1080848
[34] R. French, K. Winey, M. Yang, W. Qiu: Aust. J. Chem. 60 (2007) 251–263. DOI:10.1071/CH06222
[35] E. Palik (Ed.): Handbook of Optical Constants of Solids, Academic Press, New York, Vol. I, 1985; Vol II, 1991; Vol. III, 1998.
[36] J. Munday, F. Capasso, A. Parsegian, S. Bezrukov: Phys. Rev. A 78 (2008) 032109. DOI:10.1103/PhysRevA.78.032109
[37] V. Popov: Mat. Sci. and Eng. R 43 (2004) 61–102. DOI:10.1016/j.mser.2003.10.001
[38] C. White, J. Mintmire: J. Phys. Chem. B 109 (2005) 52–65. PMid:16850984; DOI:10.1021/jp047416+
[39] I. Cabria, J. Mintmire, C. White: Phys. Rev. B 67 (2003) 121406. DOI:10.1103/PhysRevB.67.121406
[40] P. Lambin: C. R. Physique 4 (2003) 1009–1019. DOI:10.1016/S1631-0705(03)00101-4
[41] M. Dresselhaus, G. Dresselhaus, A. Jorio, A. Filho, R. Saito: Carbon 40 (2002) 2043–2061. DOI:10.1016/S0008-6223(02)00066-0
[42] R. Saito, K. Sato, Y. Oyama, J. Jiang, G. Samsonidze, G. Dresselhaus, M. Dresselhaus: Phys. Rev. B 72 (2005) 153413. DOI:10.1103/PhysRevB.72.153413
[43] E. Barrosa, A. Joriob, G. Samsonidze, R. Capazc, A. Filhoa, J. Filhoa, G. Dresselhause, M. Dresselhaus: Phys. Rep. 431 (2006) 261–302. DOI:10.1016/j.physrep.2006.05.007
[44] A. Siber, R.F. Rajter, R.H. French, W. Ching, A. Parsegian, and R. Podgornik: Phys. Rev. B 80, (2009) 165414. DOI:10.1103/PhysRevB.80.165414

Correspondence address

Dr. Rick Rajter
Massachusetts Institute of Technology
77 Massachusetts Avenue Room 13-5046
Cambridge, MA 02139, U.S.A.
Tel.: +1 617 452 2535
E-mail: rickrajter@alum.mit.edu

Appendix A – end user checklist

As straightforward as an overall Lifshitz formulation is, much of the available literature makes it seem a complicated endeavor. This checklist can assist anyone in getting up and running.

First. Obtain the ε'' or vdW–LDS spectra for all materials present in your system. The best places to look initially are the Palik books [35], or the optical database maintained at sourceforge [19]. If those sources don't yield, attempt to find it in the available literature by searching for a material's optical properties. Ideally you need the data in either JcV or ε'' form from 0 to 30 eV. If you're still unable to find or obtain the information, you may need to collaborate with an appropriate experimentalist or ab initio scientist to get this information.

Second. Pick the analytical Lifshitz formulation that best matches your system. The best resource here is the book by Parsegian [3], which has over 100 pages devoted to every possible known analytical solution for a wide variety of geometries. If the particular geometry you are interested in does not exist, see if you can approximate it as a series of simpler geometries (far limit) or as a series of stacked planes (e. g. the Derjaguin approximation at the near limit).

Third. Does your system have multiple layers of material? If so, you may need to employ spectral mixing rules in order to adequately use a Lifshitz formulation for a given geometry. As for which particular mixing rule, analyzing the material connectivity in the direction of the interaction is the best way to get started. If the layers are stacked perfectly along this direction, a series capacitor-like mixing would be best. If exactly the opposite, one can either do a series of area weighted Hamaker coefficients of smaller pieces or apply spectral mixing with the parallel capacitor mixing method. For all arrangements in between, some EMA (Bruggeman or otherwise) will likely be the best selection.

Finally, simply use the given optical inputs within the selected Lifshitz formulation to calculate the Hamaker coefficient for the interaction. Then, multiply by the volume-volume scaling portion to get to the total vdW–Ld energy. For those not wanting to do the coding by hand, the Gecko Hamaker program available at sourceforge [19] can be used to calculate add-a-layer systems of arbitrary complexity for the plane–plane systems. At present, the SWCNTs equations have to be manually calculated in Mathematica or a programming language of your choice, but this facility will be included in an upcoming version of Gecko Hamaker.

Appendix B – total vdW–Ld energy equivalence at the far-limit

Qualitatively, the near and far limit equivalent systems can be summarized by the illustration in Fig. 14. However, a more rigorous, quantitive analysis is shown in Fig. 15 by comparing the total vdW–Ld energy ratios as a function of ℓ/d where d is the nanotube diameter. For simplicity, we calculated the Hamaker coefficient using fictitious vdW–Ld input spectra by using simple damped oscillators of the following form:

$$\varepsilon(\imath\xi) = 1 + \frac{s}{1 + \xi^2} \tag{23}$$

where s represents the magnitude or strength of the oscillator. For Fig. 15, we chose a large value of $s = 100$ for the unmixed solid material in case C3 and a value of $s = 0$ for the vacuum. For the mixture material, we used the Bruggeman effective mixing approximation (EMA) at each Matsubara frequency (the details of the EMA mixing formulation will be described more rigorously in the next section). The total energy and Hamaker coefficients were calculated using the following simple, non-retarded isotropic plane–plane equations.

$$\mathcal{G}(\ell) = \frac{\mathcal{A}}{12\pi\ell^2} \tag{24}$$

$$\mathcal{A}_{\mathcal{L}m_1/\mathcal{R}m_2} = \frac{3}{2} \sum_{n=0}^{\infty}{}' \left(\frac{\varepsilon_{\mathcal{L}} - \varepsilon_{m_1}}{\varepsilon_{\mathcal{L}} + \varepsilon_{m_1}}\right)\left(\frac{\varepsilon_{\mathcal{R}} - \varepsilon_{m_2}}{\varepsilon_{\mathcal{R}} + \varepsilon_{m_2}}\right) \tag{25}$$
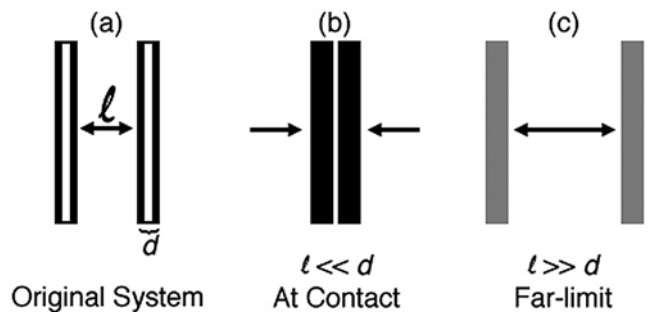

Fig. 14. The behavior of the overall effective optical properties on the Hamaker coefficient as a function of separation distance ℓ. (a) Original layered system with a thickness of 'd'. (b) At near contact ($\ell \ll d$) it is the optical properties near the respective surfaces that dominates the interaction. (c) At large separations ($\ell > 2d$), the optical properties are a weighted average of the various components and usually dominated by the materials with the larger volume fraction.
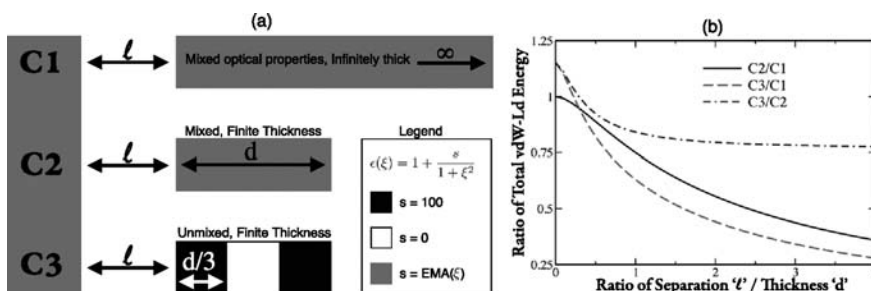

Fig. 15. Comparing total vdW–Ld interaction energy ratios of three different systems to demonstrate the utility of mixing formulations in the far-limit. (a) Case C1 uses the optically mixed material in an infinitely thick configuration. Case C2 is a finite block of the optically mixed material. Case C3 contains the unmixed material sandwiching a vacuum layer. (b) The ratio of total vdW–Ld energies varies as a function of the dimensionless scale factor ℓ/d.

Case C2 and C3 required a slightly more complicated add-a-layer form of the overall energy. We use the following (see Ref [3]) subscript notation, i.e. $\mathcal{A}_{\mathcal{L}m/\mathcal{R}m}$, so as to eliminate confusion. Here the slash in the subscript denotes the sides to the left and right of the medium. The first term in each subscript couple denotes the material furthest away from the middle/intervening separation layers. If we label the EMA mixture material as 'm', the low value vacuum as 'v', and the high value of the solid material as 'h', then the cases C1, C2, and C3 would be solved as follows.

$$C1 : \mathcal{G}(\ell) = \frac{-\mathcal{A}_{\mathrm{mv/mv}}}{12\pi(\ell)^2} \qquad (26)$$

$$C2 : \mathcal{G}(\ell) = \frac{-\mathcal{A}_{\mathrm{mv/mv}}}{12\pi(\ell)^2} + \frac{-\mathcal{A}_{\mathrm{mv/vm}}}{12\pi(\ell + d/2)^2} \qquad (27)$$

$$C3 : \mathcal{G}(\ell) = \frac{-\mathcal{A}_{\mathrm{mv/hv}}}{12\pi(\ell)^2} + \frac{-\mathcal{A}_{\mathrm{mv/vh}}}{12\pi(\ell + d/6)^2}$$
$$+ \frac{-\mathcal{A}_{\mathrm{mv/hv}}}{12\pi(\ell + 2d/6)^2} + \frac{-\mathcal{A}_{\mathrm{mv/vh}}}{12\pi(\ell + 3d/6)^2} \qquad (28)$$

Eq. (28) may look bulky, but there is a clear pattern that arises when moving from C1 to C3. In short, the total energy equation for each case is merely a summation resulting in a single term for each interface pair across the intervening medium layer. The distance part in the denominator is equivalent to the separation distance between that given pair of interfaces. The Hamaker coefficient subscripts denote the optical properties of the two neighboring materials at each of these interfaces using the ordering scheme described above (outer most material gets listed first). Thus each term can easily be constructed from the picture. As an example, the last interfaces in case C3 have a Hamaker coefficient $\mathcal{A}_{\mathrm{mv/vh}}$ at a interface–interface separation distance of $\ell + d$. It is worth noting that in cases like C2, the Hamaker coefficients are equal in magnitude but opposite in sign simply because they include the same spectra and just have their subscript order reversed. If we were to bring these interfaces completely together, the two total energy terms would cancel out as expected because the interfaces would annihilate and disappear.

At the near-limit, it is clearly the materials closest to the intervening medium that dominate the total vdW–Ld energy interaction, which is demonstrated by the C1/C2 ratio converging to 1 and thus being effectively equal despite the fact that C2 is of a finite thickness and has an additional interface term. This effective equivalence is due to the divergent, $1/\ell^2$ behavior of the nearest interface–interface pair dominating the total energy as ℓ goes to zero. In effect,

one can place any arbitrary number of interfaces at distances well beyond the leading term and they would have little to no impact on the total vdW–Ld energy. Therefore at contact, we only need to use the optical properties of the outermost layer and need not and should not use any spectral mixing.

The opposite effect occurs at the far limit. The individual Hamaker coefficients found in all four terms of case C3 are much larger than the Hamaker coefficients for case C2 because the spectral contrast at each interface in C3 is much greater. One might be too quick to conclude that these larger Hamaker coefficients should lead to a larger total energy for case C3 as compared to C2. However the interfaces in C3 begin to pack more closely and thus the overall magnitudes of the $1/\ell^2$ terms (i.e. the geometrical components) of the neighboring interfaces get closer. These two effects (increasing Hamaker coefficients and decreased spacing) cancel each other out making cases C2 and C3 nearly identical in the far limit, with case C2 certainly giving us an advantage of reduced complexity.

Figure 15b illustrates these effects. Additionally it is important to note that ratio of C3/C2 converges to a fixed value when $\ell > d$, where d is the thickness of the finite layers in cases C3 and C2. This particular distance of convergence is an encouraging result because it is the exact same distance we determined to be the far limit regime in our analysis of the anisotropic solid-cylinder Lifshitz formulations. For the purposes of stress-testing the EMA mixing rules, we purposely chose extreme values of 's' to mimic the vacuum (v: $s = 0$) and metal (h: $s = 100$) endpoints. Therefore this 23 % discrepancy can be thought of as the maximum error that can exist between the total vdW–Ld energies of cases C2 and C3 in the far limit. If we were to pick values of 's' that were closer in value to each other (e. g. v: $s = 50$ and h: $s = 100$), then the difference in total energy drops to less than 4 %. And of course, if materials 'v' and 'h' have identical spectra, the ratio of C2/C3 merges to unity at the far limit. Therefore, one can confidently mix spectra that are on the same order of magnitude and be sure they are getting realistic results. When spectra are vastly different, there will be some discrepancies that need to be taken into account.

There is one final issue to note in Fig. 15. Although the limit separation regimes are easy to characterize, there is a transition range between the near and far limits which is harder to define. For those cases, one might best use the interpolation method described previously in order to get a reasonable Hamaker coefficient and total vdW–Ld energy at any separation distance. This process is beyond the scope of this paper, which is primarily focused on the effects of mixing on the limiting behaviors. However those wishing to know this information within this regime can do so in a reasonably straightforward manner [7].